Quantification of amyloid fibril polymorphism by nano-morphometry reveals the individuality of filament assembly

Liam D. Aubrey [1†], Ben J. F. Blakeman [1†], Liisa Lutter [1], Christopher J. Serpell [2], Mick F. Tuite [1], Louise C. Serpell [3], Wei-Feng Xue [1*]

[1] Kent Fungal Group, School of Biosciences, University of Kent, CT2 7NJ, Canterbury, UK

[2] School of Physical Sciences, University of Kent, CT2 7NH, Canterbury, UK

[3] Sussex Neuroscience, School of Life Sciences, University of Sussex, BN1 6NN, Falmer, Brighton, UK

[†] Authors contributed equally to this study

* Correspondence to: W.F.Xue@kent.ac.uk; Tel +44-(0)1227 824821

Key words: amyloid / fibril structure / polymorphism / self-assembly / atomic force microscopy / image analysis

ABSTRACT

Amyloid fibrils are highly polymorphic structures formed by many different proteins. They provide biological function but also abnormally accumulate in numerous human diseases. The physicochemical principles of amyloid polymorphism are not understood due to lack of structural insights at the single-fibril level. To identify and classify different fibril polymorphs and to quantify the level of heterogeneity is essential to decipher the precise links between amyloid structures and their functional and disease associated properties such as toxicity, strains, propagation and spreading. Employing gentle, force-curve based AFM, we produce detailed images, from which the 3D reconstruction of individual filaments in heterogeneous amyloid samples is achieved. Distinctive fibril polymorphs are then classified by hierarchical clustering, and sample heterogeneity is objectively quantified. These data demonstrate the polymorphic nature of fibril populations, provide important information regarding the energy landscape of amyloid self-assembly, and offer quantitative insights into the structural basis of polymorphism in amyloid populations.

INTRODUCTION

Amyloid fibrils are well known for their association with protein misfolding diseases, collectively known as Amyloidoses, as well as several neurodegenerative disorders. Each disease is characterised by a specific protein that accumulates in the peripheral tissues, in peripheral organs or in the brain. All amyloid fibrils have a core cross-β molecular architecture composed of β strands that stack perpendicular to the long fibril axis to form protofilaments up to several microns in length [1]. Multiple protofilaments can laterally associate to form twisted fibrils with a hydrophobic core [2,3]. Alzheimer's Aβ is one of the best known of the amyloid proteins, others include islet amyloid polypeptide in diabetes type 2 [4], β-2 microglobulin in dialysis related amyloidosis [5–7], transthyretin in familial amyloidotic polyneuropathy [8,9] amyloid A (AA) in acute phase amyloidosis [10], tau in Alzheimer's and other tauopathies, and α-synuclein in Parkinson's disease [11]. There are also many known amyloid forming proteins that are not associated with disease but with biological function, including structural components of biofilms such as Curli expressed in *E. coli*, [12,13] and amyloid fibrils involved in human skin pigmentation such as Pmel17 [14,15].

Advances in high resolution structural determination techniques such as X-ray crystallography, solid-state nuclear magnetic resonance (ssNMR) and cryo-transmission electron microscopy (cryo-EM) have recently revolutionised our understanding of amyloid fibril structures [16–19]. For example, recent cryo-EM and ssNMR structures of Aβ [17,20,21] and tau [16,22,23] reveal parallel, in register organisation of the proteins within the cross-beta core. These advances provided molecular information on the 3D fold of the monomeric subunits within the core of distinct fibril types in addition to information about the intermolecular interactions between amino acid

residues [24]. The impact of mutations on the core fold, for example in familial forms of Alzheimer's disease, can therefore be accessed [20]. Thus, on an atomic scale, these techniques have advanced our understanding of the core structures that make up individual amyloid fibril types.

On a mesoscopic (micrometre to nanometre) scale, amyloid fibrils display a high degree of polymorphism and amyloid populations are often highly heterogeneous. This has been demonstrated in disease related amyloid fibrils in both *in vitro* and *ex vivo* samples, as well as in samples of functional amyloid [25–27]. For example in a study involving Aβ, ssNMR data was compared for fibril structures taken from various patients which showed that the structures of the fibrils observed were highly varied from patient to patient in both $A\beta_{1\text{-}40}$ and $A\beta_{1\text{-}42}$ [28]. Structural characterisation has revealed that many amyloidogenic proteins can form polymorphic structures, revealing that, for example, AA can fold into different conformations dependent on the species as well as the individual patients [29], while tau has been shown to form different polymorphs in different tauopathies [16,22,30].

Structural polymorphism in amyloid fibrils, can be dependent on the number and orientation of the protofilaments that are arranged within a fibril [31], as well as the conformation of the monomeric subunits that make up the core of the fibril structure which is in turn dependent on the primary sequence [32]. Fibril structural polymorphism can be identified by the twists along the longitudinal axis of the fibrils producing varied periodic cross-over distances, and by the shape and size of the cross-sectional area of the fibril [33]. Polymorphism is of interest due to the possibility that different fibril polymorphs may have different physical properties, such as the rate of fragmentation [34,35] or the ability to act as a catalytic surface for secondary nucleation [35,36]. Different physical properties could in turn result in different biological activities, such as the

92 potential to propagate in a prion-like manner [37], the ability to associate with cytotoxic active
93 species [38] or the impermeability of a biofilm matrix [39]. Another example of an amyloid structure
94 function relationship is demonstrated by the difference in the structures of murine and human
95 AA which results in a lower efficiency for the induction of amyloidosis between species [29].
96 Using electron microscopy (EM) and atomic force microscopy (AFM), it has been possible to
97 observe and differentiate between polymorphs in amyloid fibril samples [27]. However, since
98 fibril polymorphism has generally only been assessed in a qualitative manner with respect to
99 the overall heterogeneity of amyloid fibril data sets [27], the structural, physicochemical and
100 mechanistic origin of polymorphism, the extent to which it exists and its effect on biological
101 activity is not known.
102
103 In order to identify, classify and quantify amyloid fibril polymorphism, as well as enumerate
104 the heterogeneity of amyloid samples, the structure of individual fibrils in a sample population
105 must first be resolved at sufficiently high-resolution so that individual twist patterns, twist
106 handedness and cross-sectional profiles are distinguishable at a single-fibril level without
107 cross-filament averaging. Here, using a force-curve based AFM imaging at low contact forces,
108 we are able to image, in sufficiently high detail, individual fibrils made from three different
109 peptides with sequences HYFNIF, VIYKI and RVFNIM. These peptides are short
110 amyloidogenic sequences originating within larger proteins (Human Bloom syndrome protein,
111 Drosophila Chorion protein and Human elF-2, respectively [40]) identified via the Waltz
112 algorithm [41]. Structural models of the amyloid protofilament cores from the Waltz peptide
113 assemblies have been presented previously (**Figure 1**) which were validated using X-Ray Fibre
114 Diffraction (XRFD) data, but these assembly reactions have also been previously observed to
115 produce a large range of fibril polymorphs upon assembly [40]. Thus, they provide excellent
116 model systems for investigating the structural basis of polymorphism within amyloid

populations. Here, using the AFM image data sets collected, each individual fibril observed in AFM images were reconstructed as a distinct 3D model, and the structural parameters of individual fibrils in the sample populations were measured and compared. Finally, we employed an agglomerative hierarchical clustering method to classify fibril polymorphs by measuring the structural differences observed between individual fibrils. The results show that variation in the degree of structural polymorphism and the heterogeneity of amyloid fibril samples are highly sequence specific. More importantly, the data and analysis here demonstrate that that each individual amyloid fibril has characteristics that are different to those of the population average.

RESULTS

Gentle force-curve based AFM imaging identifies distinct fibril polymorphs to high detail

Considerable heterogeneity has been displayed in several amyloid fibril samples previously [26,27], including in samples made from Waltz peptide amyloid assembly reactions [40]. To achieve the high level of detail required for quantitative structural analysis for individual amyloid fibrils without cross-particle averaging, we imaged the three Waltz peptide assembly samples, HYFNIF, RVFNIM and VIYKI, using a force-curve based AFM imaging method. AFM is a high signal-to-noise method that has been used previously to image amyloid fibrils at high resolution [42–45]. Here, force-curve based imaging (Peak-force tapping mode, Bruker) was employed rather than traditional tapping mode imaging so that the force applied to the sample was kept consistent and minimal ensuring that the specimens were not deformed and that the surface details were tracked faithfully. Typical images of the three Waltz peptide assembly

142 samples collected using force-curve based imaging are shown in **Figure 2**. Closer inspection
143 of these images shows that fine details such as the length and handedness of repeating patterns
144 in the fibrils can be readily observed without any further processing of the raw image data.
145 Qualitatively, it is clear that there is a high degree of heterogeneity in these samples since many
146 fibrils of different heights and twist patterns, including some with different handedness can be
147 observed from within the same image.
148
149 Around 90 well-separated fibrils for each of the Waltz peptide assemblies were chosen from
150 the images. Their contours along the filament centres where individually traced and digitally
151 straightened. **Figure 3** shows eight typical 500 nm long fibril segment examples from each of
152 the three data sets (almost all traced fibrils were longer than 500 nm, only a portion of the traces
153 are shown in **Figure 3**). All three peptide precursors result in a set of visibly distinguishable,
154 unique fibrils. All of the traced fibrils are displayed in **Supplementary Figure SI 1**.
155
156 **3D models of each individual amyloid fibril in the heterogeneous samples can be**
157 **reconstructed**
158
159 An informative method for visualising and comparing polymorphic filament structures in high
160 detail is to reconstruct 3D models of the filaments from the AFM image data. In this case,
161 because AFM is a high signal-to-noise imaging method, we were able to reconstruct 3D
162 structural models with sufficient detail without averaging across multiple filaments, thus
163 producing individual models for each of the traced fibrils. 3D reconstruction also allows for
164 visualising and comparing filament structures without the influence of the varying degree of
165 tip-sample convolution on the AFM images due to varying cantilever tip dimensions across
166 different images (evident in the varied apparent width of the fibrils within the images in **Figure**

167 **3**). **Figure 4** shows examples of the 3D fibril models from the three data sets. All 266 models
168 are shown in **Supplementary Figure SI 2**. In addition, the 3D models reveal the shape and
169 size of the cross-section of each of the fibrils and how the cross-section rotates along the length
170 of the fibril (**Supplementary Figure SI 3**). In this respect, the VIYKI data set stands out as all
171 of the fibril models show near-circular cross-sections. This is particularly striking when
172 compared to the HYFNIF and RVFNIM data sets in which there are numerous fibril types with
173 ellipsoidal cross-sections as well as a few models which display asymmetric features. In
174 summary, all three datasets display fibrils with varying degree of structural individualities, and
175 a range of polymorph classes that can be distinguished qualitatively.
176
177 **Analysis of height, twist periodicity and cross-sectional area enables the quantification of**
178 **heterogeneity due to fibril polymorphism**
179
180 Identifying the fibril polymorphs at the level of individual fibrils led to the qualitative
181 observation that all three samples display a high degree of heterogeneity. In order to quantify,
182 enumerate and compare the overall heterogeneity of the samples, we performed nano-
183 morphometric measurements on individual filaments in our datasets. For each of the ~90 fibrils
184 from each of the three datasets, six different structural parameters where measured
185 (**Supplementary Table 1, Figure 5**): maximum height (h_{max}), minimum height (h_{min}), average
186 height (h_{mean}), handedness, periodic frequency, and average cross-sectional area (*csa*). The
187 periodic frequency refers to the frequency of the most common repeating pattern observed in
188 the height profile of a straightened filament identified by Fast Fourier Transform (FFT) of the
189 height profile, corresponding to the twist pattern of the filaments. The frequency of the
190 periodicity per nm was used rather than the periodicity as this would allow any twisted "ribbon"
191 like fibrils with very long twist periodicity to be analysed and visualised in the same way as

192 fibrils with a very short periodicity. The handedness of the twist was determined separately by
193 manual inspection of the fibril images and 2D Fourier transform (2D power spectral density
194 map) of the fibril images. The periodic frequency of fibrils with left-handed twists were
195 assigned negative frequency values while the periodic frequency of right-handed twisted fibrils
196 retained positive values to give directional periodic frequency (*dpf*) values that enabled the
197 visualisation of the distribution between left and right handedness in each data set. The standard
198 deviation (SD) of the 5-dimensional (h_{mean}, h_{max}, h_{min}, *dpf* and *csa*) Euclidian distance to the
199 global mean for each dataset was subsequently calculated as a quantitative measure of sample
200 heterogeneity (Equation 2 in Materials and Methods). For the three peptide sequences studied
201 here, VIYKI peptide assembly showed the most structural heterogeneity with a SD of 2.57,
202 RVFNIM had a SD of 1.98 and HYFNIF showed the least structural heterogeneity with a SD
203 of 1.40.
204
205 In order to display the whole fibril population of morphometric measurements, the average
206 height was plotted against the directional periodic frequency as a contour map which is shown
207 in **Figure 6**. The contours represent the density of the data in specific regions (seen as two-
208 dimensional projections in **Figure 6**). The information gained from the contour map is
209 analogous to a plot of an energy landscape for the assembly reactions where deeper energy
210 wells represent more likely structures. As shown in **Figure 6**, both HYFNIF and VIYKI peptide
211 assembly reactions appear to be dominated by the formation of left-handed twisted fibrils.
212 Interestingly, in contrast, RVFNIM peptide assembly displays no overall dominant preference
213 for twist handedness. There is, therefore, a sequence specific energetic favourability for
214 forming predominantly left-handed or right-handed fibrils. In contrast to RVFNIM and VIYKI,
215 HYFNIF fibril polymorphs were mostly populated in one narrow region of the contour map
216 with a few outliers, suggesting that there was a deeper preference for one class of assembly

compared to the other two sequences. Fibrils made from the VIYKI peptide however, covered a large range of polymorphs with different average heights and periodic frequencies, populating a large area in the contour diagram in **Figure 6**, suggesting that there were multiple classes of structure that were almost equally likely to occur, and therefore similar in terms of the free energy associated with protofilament assembly. RVFNIM fibrils displayed an intermediate level of heterogeneity, with some preference for specific classes of both left-hand and right-hand twisted polymorphs. On a contour plot of the minimum height vs the maximum height, shown in the **Supplementary Figure SI 4**, VIYKI fibrils showed a tendency to have more similar values for minimum and maximum heights suggesting a preference for cross-sections with a particularly rounded shape whereas HYFNIF and RVFNIM assembled into fibrils that may have a larger maximum height than minimum height. This was also observed when the average cross-sectional areas of the models were plotted against the average height of the fibrils where the cross-sectional areas of VIYKI fibrils are distributed close to the line expected for circular cross-sections (cross-sectional area proportional to width squared). These observations support the qualitative assessment of the models in which the VIYKI fibrils overall appear to be more cylindrical. In summary, the three different assembly reactions, despite all resulting in amyloid fibrils with cross-beta core, display different assembly free energy landscapes, which are influenced by their side chain composition. This results in sequence specific preferences in the polymorphs that they form (e.g. in terms of width, twist and handedness) is due to variations in the packing of the side-chains within the protofilaments, the packing of the protofilaments in the fibrils or a combination of both, and results in differences in the heterogeneity of the fibril populations.

Amyloid fibril polymorphs can be classified by hierarchical clustering

Classifying fibril polymorphs within a sample population can provide visualisation and organisation of the single-fibril level structural data that allows for further analysis of the activities and behaviours of types of structural polymorphs. Here, natural divisions in the data set of amyloid fibrils can be found by identifying which fibrils have shared or similar features and which fibrils do not, as determined by the nano-morphometric measurements. Subsequently, agglomerative or 'bottom-up' hierarchal clustering was performed to resolve the natural divisions within each dataset and therefore objectively classify the fibrils. The standardised Euclidean distance between each possible pair of fibrils in 5-dimensions (average height, maximum height, minimum height, directional periodic frequency and cross-sectional area), was calculated and linked together iteratively to generate a linked tree representing the structural and morphological relationships between individual fibrils. The morphometric data can then be represented in a dendrogram with the clusters on the x-axis and the 5-dimensional standardised Euclidian distance from one cluster to the next on the y-axis. In the **Supplementary Figure SI 5**, full dendrograms displaying the entire trees of the three datasets are presented. In order to separate the fibrils into 'classes', the data must be analysed at appropriate distance cut-offs. The distance cut-off determines the maximum distance within any clusters (or class). Therefore, the number of clusters at a given distance cut-off is indicative of the heterogeneity of the data set. A greater number of clusters suggest that the data is more spread out and therefore more heterogeneous. The dendrograms shown in **Figure 7a** have been collapsed based on a distance cut-off of 1 (standardised Euclidean distance) show how the datasets were subsequently classified in **Figure 7b and 7c**.

In total, at a distance cut-off of 1 in the standardised 5-dimensional Euclidean space, 13 separate clusters were generated by HYFNIF polymer assembly, 22 clusters were generated by RVFNIM polymer assembly and 19 clusters were generated by VIYKI polymer assembly.

These clusters can be seen as classes of fibrils, where member fibrils of the same class show similar structure in terms of their morphometric appearances. Further analysis of the data at different distance cut-offs, shown in **Supplementary Figure SI 6**, corroborate that HYFNIF fibrils display considerably less heterogeneity than RVFNIM and VIYKI. Interestingly, when compared to VIYKI, the RVFNIM data appears to be spread more evenly resulting in larger number of clusters compared to VIYKI despite showing smaller distance SD value. This suggests that VIYKI forms fibril classes that are very different but structurally and energetically similar within each class, whereas the RVFNIM fibrils are overall more similar across fibril classes compared to VIYKI fibrils. This may indicate that the energy landscape for the assembly reaction is flatter and more rugged for RVFNIM so that the structural differences between possible RVFNIM fibril polymorphs are on a more continuous scale compared with VIYKI fibrils with distinct but distant polymorphs.

DISCUSSION

High-resolution images of amyloid fibril samples assembled from three amyloidogenic peptide sequences using a gentle, force-based AFM approach allowed for the detailed quantitative structural identification of polymorphs at a single fibril level. Individual 3D reconstructed fibril models were made for every traced fibril in the data set which included ~90 fibrils from each peptide assembly and 266 fibrils in total. This demonstrates the utility of AFM as an imaging method for the structural analysis of amyloid fibril populations at the single fibril level, and is highly complementary to cryo-EM methodologies. Morphometry is the process of measuring differences in the structures of objects and is often performed to measure differences in anatomy such as physiological differences in the brain [46,47]. Here, we perform quantitative nano-

morphometric measurements on individual fibrils in heterogeneous amyloid samples. Using our AFM data, we were able to make quantitative measurements of different structural parameters which allowed us to distinguish between different polymorphs of amyloid fibril structure. Indeed, the data shows that each fibril in the amyloid samples is unique. The advances reported here opens up the future possibility of analysing and comparing the structures present in entire populations of amyloid fibril species on a single fibril level, thereby opening up the possibility of linking population level and single fibril level properties. This connection may be key in order to decipher the relationships between specific polymorphs or structural properties and phenotypic behaviours or biological consequences of amyloid.

The overall heterogeneity of the samples made from each different Waltz peptide precursor was quantified and enumerated. These results also provide an indication of the energy landscape associated with the filament assembly reaction of each peptide. In the cases compared here, it was revealed that VIYKI assembly resulted in an overall more heterogeneous population than the other two peptides and that VIYKI and HYFNIF fibril assemblies are dominated by the formation of left-handed fibrils, whereas RVFNIM assemblies shows no overall preference to handedness as similar sized populations of both left-hand and right-hand twisted fibrils were formed. It has been thought that left-handed predominance in amyloid fibrils is a result of the natural curvature of the β-strands that make up the monomeric subunits which comes from the backbone of the polypeptide chains from L-amino acids [48]. The results here supports the idea that preference for left-handedness is not absolute and the preference for handedness could be modulated by side-chain sequence [49,50]. In this case, the side-chains in RVFNIM assemblies may counteract the natural curvature of the β-strand due to the influence of specific side chains interactions in some polymorphic arrangements. Overall, the specific energetic explanation for the difference in behaviour between the three peptide assemblies

317 remains unknown. However, the data here demonstrate the considerable influence of amino
318 acid sequence in filament assembly reactions and opens up the possibility of systematic
319 sequence-structure analysis of cross-β assemblies. Furthermore, utilising an agglomerative
320 hierarchical clustering approach, we were able to objectively assign individual fibrils to
321 different classes of fibril polymorph. By analysing the dendrograms that allowed visualisation
322 of the similarities and dissimilarities between individual fibrils, it was possible to identify the
323 natural divisions in the datasets and existence of clusters that existed in the data. This
324 information was then used to classify individual fibrils to a cluster. The number of clearly
325 defined clusters also corroborated the overall heterogeneity of the data sets. The distance
326 between the fibril classes may also reflect the possible plasticity of the types of polymorph
327 observed in each data set. For example, VIYKI fibrils are likely belong to a predominant type
328 of polymorph, which is very different to any other type of possible VIYKI fibril polymorph.
329 As a consequence, such a population if presented in biological context may not be able to shift
330 to a different polymorph easily under pressure from environmental changes. The most common
331 types of HYFNIF fibril, however, are very similar and so HYFNIF fibril populations may be
332 able to shift their morphology much more easily when conditions change. Thus, this work
333 demonstrates a general utility to quantify polymorphism in amyloid fibril data sets by AFM on
334 a single fibril level as a possible means to quantify and comparing fitness of individual amyloid
335 or prion polymorphs under any given set of conditions.
336
337 Structural polymorphism could account for some of the biological activities associated with
338 amyloid observed *in vivo*. Individual fibril polymorphs will have different physical properties.
339 For example, thicker fibril polymorphs with a circular cross section will have a different second
340 moment of inertia compared to thin polymorphs with a more oval shaped cross section, which
341 could result in differential stability to fibril fragmentation. Thicker fibrils with large surface

areas per length may provide more sites for secondary nucleation events than thinner fibrils with small surface areas. Thus, fibril polymorphs displaying different properties would likely have different biological activities, even formed from identical precursors and present within the same population. In this case, individual fibrils within a population may also have higher rates of fragmentation that could result in a greater likelihood for propagation [51,52] or cytotoxicity [34], or higher rates of secondary nucleation that could result in more cytotoxic active species [38]. Various proteins and peptides with different amino acid sequences are amyloidogenic [53]. Yet, despite all of them being capable of forming amyloid fibrils *in vivo*, they display different biological activities [54–56]. Therefore, the variation in heterogeneity caused by polymorphism, as well as individual polymorphs could account for the differences in biological activity between different amyloidogenic precursors.

Prion and prion-like amyloid fibrils are able to propagate between cells [57,58]. Segregation of specific fibril polymorphs could result in the cell-specific propagation of polymorphs [59] likely manifest as strains in mammals or variants in yeast. This could result in different biological activities in different cells infested with the same amyloid sample. Examples of this include the identification of numerous strains of Tau, each of which causes a different pathology, in different brain regions and propagates at different rates [60] and the identification of two α-synuclein strains which show the same type of strain dependent phenomena [58]. This is of particular importance as some fibril polymorphs may react differently to potential inhibitors, which could result in strains that become 'resistant' to therapeutics over time. The strains phenomenon seen in prions and prion-like amyloid, in which structural characteristics presumably determine the biological activity of the fibrils has been demonstrated in human prions [61]. This behaviour has also been implicated in the Alzheimer's related Aβ peptides [62]. It is, therefore, important to investigate amyloid polymorphism in heterogeneous populations

from a single fibril perspective, as this can account for differences in specific constructive or destructive biological activities associated with amyloid structures since each individual amyloid fibril particle has characteristics that may be vastly different to those of the population average.

MATERIALS AND METHODS

Waltz Peptide synthesis

The Waltz peptides with the sequences HYFNIF, RVFNIM and VIYKI were purchased from JPT peptide technologies, or the Biomolecular analysis facility at the University of Kent. The peptides were synthesised with N-terminal acetylation and C-terminal amidation. Multistage solid phase synthesis using Fmoc protection chemistry generated a lyophilised powder with > 95% purity as measured by HPLC.

In vitro polymerisation

To prepare amyloid fibril samples formed from the three Waltz peptides, 1 mg of the respective lyophilised powder was dissolved in 100 µl of filter sterilized milli-Q water to a final concentration of 10 mg/ml. The solution was incubated at room temperature for 1 week prior to imaging. This allowed for the 'maturation' of the fibrils from all three Waltz peptide samples to occur within a standardised amount of time.

AFM sample preparation and imaging

Each Waltz peptide assembly sample was diluted to 0.05 mg/ml in a dilute solution of HCl (pH 2.0, made up using filter sterilised milli-Q water). Immediately after dilution, 20 µl samples

were deposited onto freshly cleaved mica surfaces (Agar scientific, F7013) and incubated for 10 minutes. Following incubation, the sample was washed with 1 ml of filter sterilised milli-Q water and then dried using a stream of nitrogen gas. Fibrils were imaged using a Multimode AFM with a Nanoscope V (Bruker) controller operating under peak force tapping mode using ScanAsyst probes (silicon nitride triangular tip with tip height = 2.5-2.8 μm, nominal tip radius = 2 nm, nominal spring constant 0.4 N/m, Bruker). Each collected image had a scan size of 6 x 6 μm and 2048 x 2048 pixels or 12 x 12 μm and 4096 x 4096 pixels. A scan rate of 0.305 Hz was used with a noise threshold of 0.5 nm and the Z limit was reduced to 1.5 μm. The peak force set point was set automatically, typically to ~675 pN during image acquisition. Nanoscope analysis software (Version 1.5, Bruker) were used to process the image data by flattening the height topology data to remove tilt and scanner bow.

Structural data extraction

Fibrils were traced [63] and digitally straightened [64] using an in-house application and the height profile for each fibril was extracted from the centre contour line of the straightened fibrils. The periodicity of the fibrils was then determined using fast-Fourier transform of the height profile of each fibril. Some fibrils do not display any clear periodicity and have a height profile that appears to show an erratic pattern so frequency of the highest peak in the frequency domain per nm was used. The final datasets consist of a varying multitude of images comprising ~90 individually traced fibrils per Waltz sequence. The same pixel density is maintained for all images within the dataset.

3D modelling of fibril structures

Straightened fibril traces were corrected for the tip-convolution effect using an algorithm based on geometric modelling of the tip-fibril contact points (Lutter et al., 2019a, in preparation).

Briefly, the variation in the tip radius from their nominal value was first determined. Tip radii can be estimated by imaging standards such as gold nanoparticles with known dimensions [66]. It is also important to consider that the tip can become blunter with scanning action and the tip radius can widen over time. Therefore, the tip radius was estimated for each individual fibril on an image from the extent of convolution seen in data by assuming the twisted amyloid fibrils have ideal corkscrew symmetry with circular average cross-section of the fibril perpendicular to its axis of rotation. The algorithm then corrects for the lateral dilation of nano-structures resulting from the finite dimensions of the AFM probe, without the loss of structural information, by resampling of the fibril images to tip-sample contact points. This results in recovering subpixel resolution of lateral sampling. Each pixel value in the straightened fibril data is then corrected in their x, y and z coordinates. Filament helical symmetry was estimated by building 3D models with various symmetries from the data, back calculating a dilated AFM image and comparing the angle of the fibril twist pattern with that of the straightened fibril trace in the simulated images and in the 2D Fourier transform of the simulated images. Then for construction of the 3D models, the degree of twist per pixel along the y-axis was found by dividing 360° with the product of fibril periodicity and its symmetry number (e.g. 1 2 or 3 etc.). The 3D models were made assuming a helical symmetry using a moving-window approach, in which a window, centred at a pixel n, contained the pixels $n - x$ to $n + x$ where x is the axial length covered by 180° twist. The central pixel n is not rotated while neighbouring pixels on both sides along the y-axis are rotated by a rotation angle, which is the product of the twist angle and the distance from n in pixels. Rotation angle values are negative in one direction from n and positive in the other direction, with the specific direction depending on the handedness of the fibril, determined by manual inspection of the straightened fibril image and its 2D Fourier transform image.

Nano-morphometric measurements on individual fibrils

Fibril image datasets for RVFNIM, HYFNIF and VIKYKI were analysed with 92, 89 and 85 individually traced and characterised fibrils, respectively. Five morphometric parameters were extracted from the image data for each of the fibrils and the 3D models of the individual fibrils as shown in **Figure 5** The maximum, minimum and average heights were measured on the central ridge of each fibril. The periodic frequencies were obtained by Fourier-transform of the z-coordinates along the central ridge of each fibril. The average cross-sectional areas were obtained by averaging of the numerical polar integration along the fibril axis of the reconstructed fibril 3D models.

Hierarchical Clustering

The standardised Euclidean distance *d(x, y)* in 5-dimensional space representing the five morphometric parameters average height, maximum height, minimum height, directional periodic frequency and average cross-sectional area (each data point consists of these five values, representing a single fibril segment) was calculated for every possible pair of data points (e.g. fibrils x and y) using equation (1) where *V* is the 5-by-5 diagonal matrix whose *j*th diagonal element is the variance (standard deviation squared) for each of the five morphometric parameters. In Equation (1), x and y are 1 by 5 row vectors representing each of the data points, with the elements in the vectors representing each of the 5 morphometric parameters for each individual fibril. Here, the diagonal elements of the V matrix contain the list of the variance for each parameter individually across all 3 data sets.

Equation (1)

$$d(x,y) = \sqrt{(x-y)V^{-1}(x-y)'}$$

As expressed in Equations (1), therefore, the Euclidian distances are standardised by dividing the distance in each of the morphometric parameter with their global standard deviation. Hence,

the standardised Euclidean distance, d, between two fibril data-points is a unitless measure of the similarity (or dissimilarity) between the two. The distance standard deviation *SD* of the morphometric data as a measure of the heterogeneity of the fibril populations was defined as the standard deviation of $d(x, \bar{x})$, which is the standardised Euclidean distance between each of the data points and the mean of all the data points, as shown in equation (2).

Equation (2)

$$SD = \sqrt{\frac{\sum_{i=1}^{n}(d(x_i, \bar{x}))^2}{n-1}}$$

In Equation (2), n is the total number of data points. Agglomerative hierarchical clustering was performed using the average linkage function shown in equation 3, which hierarchically links clusters using the average distance between all pairs of data points in any two clusters.

Equation (3)

$$d(r,s) = \frac{1}{n_r n_s}\sum_{i=1}^{n_r}\sum_{j=1}^{n_s} d(x_{ri}, x_{sj})$$

In Equation (3), *d(r, s)* is the average distance between cluster r with n_r data points and cluster s with n_s data points. Explained briefly, the shortest distance between any two data points within a data set is found. Those two data points are then considered to be a cluster, and the average coordinate of the two data points in the 5-dimensional space is used as the coordinate of the cluster. This is then repeated until all of the data is linked under one cluster.

AUTHOR CONTRIBUTIONS

L.D.A. and B.J.F.B. designed the research, conducted the experiments, and analyzed the data. L.L. wrote the analytical software tools. C.J.S. and M.F.T. designed the research and analyzed the data. L.C.S. designed the research, provided assembly reagents and methods, and analyzed

the data. W.F.X. designed the research, wrote the analytical software tools, analyzed the data, and managed the research. The manuscript was written through contributions of all authors.

ACKNOWLEDGEMENTS

We thank the members of the Xue group, the LCS group, the CJS group and the Kent Fungal Group for helpful comments throughout the preparation of this manuscript. We also thank Ian Brown and Kevin Howland for technical support. This work was supported by funding from the University of Kent (B.J.F.B), Biotechnology and Biological Sciences Research Council (BBSRC), UK grant BB/S003312/1, as well as Engineering and Physical Sciences Research Council (EPSRC), UK DTP grant (EP/R513246/1 for L.L).

REFERENCES

1. Sunde, M. *et al*. Common Core Structure of Amyloid Fibrils by Synchrotron X-ray Diffraction. 11 (1997).
2. Jiménez, J. L. *et al*. The protofilament structure of insulin amyloid fibrils. *Proc. Natl. Acad. Sci. U. S. A.* **99**, 9196–9201 (2002).
3. Serpell, L. C. *et al*. The protofilament substructure of amyloid fibrils. *J. Mol. Biol.* **300**, 1033–1039 (2000).
4. Raleigh, D., Zhang, X., Hastoy, B. & Clark, A. The β-cell assassin: IAPP cytotoxicity. *J. Mol. Endocrinol.* **59**, R121–R140 (2017).
5. Iadanza, M. G. *et al*. The structure of a β 2 -microglobulin fibril suggests a molecular basis for its amyloid polymorphism. *Nat. Commun.* **9**, 1–10 (2018).

514 6. Iwata, K. *et al*. 3D structure of amyloid protofilaments of β2-microglobulin fragment
515 probed by solid-state NMR. *Proc. Natl. Acad. Sci. U. S. A.* **103**, 18119–18124 (2006).
516 7. Stoppini, M. & Bellotti, V. Systemic Amyloidosis: Lessons from β2-Microglobulin. *J. Biol.*
517 *Chem.* **290**, 9951–9958 (2015).
518 8. Teng, M. H. *et al*. Amyloid and nonfibrillar deposits in mice transgenic for wild-type
519 human transthyretin: a possible model for senile systemic amyloidosis. *Lab. Investig. J.*
520 *Tech. Methods Pathol.* **81**, 385–396 (2001).
521 9. Zhao, L., Buxbaum, J. N. & Reixach, N. Age-related oxidative modifications of
522 transthyretin modulate its amyloidogenicity. *Biochemistry* **52**, 1913–1926 (2013).
523 10. Rokita, H., Shirahama, T., Cohen, A. S. & Sipe, J. D. Serum amyloid A gene expression
524 and AA amyloid formation in A/J and SJL/J mice. *Br. J. Exp. Pathol.* **70**, 327–335 (1989).
525 11. Goedert, M. Alpha-synuclein and neurodegenerative diseases. *Nat. Rev. Neurosci.* **2**, 492–
526 501 (2001).
527 12. Deshmukh, M., Evans, M. L. & Chapman, M. R. Amyloid by Design: Intrinsic Regulation
528 of Microbial Amyloid Assembly. *J. Mol. Biol.* **430**, 3631–3641 (2018).
529 13. Erskine, E., MacPhee, C. E. & Stanley-Wall, N. R. Functional Amyloid and Other Protein
530 Fibers in the Biofilm Matrix. *J. Mol. Biol.* **430**, 3642–3656 (2018).
531 14. Jackson, M. P. & Hewitt, E. W. Why are Functional Amyloids Non-Toxic in Humans?
532 *Biomolecules* **7**, 71 (2017).
533 15. Watt, B., Niel, G. van, Raposo, G. & Marks, M. S. PMEL: a pigment cell-specific model
534 for functional amyloid formation. *Pigment Cell Melanoma Res.* **26**, 300–315 (2013).
535 16. Fitzpatrick, A. W. P. *et al*. Cryo-EM structures of tau filaments from Alzheimer's disease.
536 *Nature* **547**, 185–190 (2017).
537 17. Gremer, L. *et al*. Fibril structure of amyloid-beta(1-42) by cryo-electron microscopy.
538 *Science* **358**, 116-+ (2017).

539 18. Guerrero-Ferreira, R. *et al*. Cryo-EM structure of alpha-synuclein fibrils. *eLife* **7**, e36402
540 (2018).
541 19. Eisenberg, D. S. & Sawaya, M. R. Structural Studies of Amyloid Proteins at the Molecular
542 Level. *Annu. Rev. Biochem.* **86**, 69–95 (2017).
543 20. Wälti, M. A. *et al*. Atomic-resolution structure of a disease-relevant Aβ(1–42) amyloid
544 fibril. *Proc. Natl. Acad. Sci.* **113**, E4976–E4984 (2016).
545 21. Tycko, R. Molecular Structure of Aggregated Amyloid-β: Insights from Solid-State
546 Nuclear Magnetic Resonance. *Cold Spring Harb. Perspect. Med.* **6**, (2016).
547 22. Falcon, B. *et al*. Novel tau filament fold in chronic traumatic encephalopathy encloses
548 hydrophobic molecules. *Nature* **568**, 420–423 (2019).
549 23. Falcon, B. *et al*. Tau filaments from multiple cases of sporadic and inherited Alzheimer's
550 disease adopt a common fold. *Acta Neuropathol. (Berl.)* **136**, 699–708 (2018).
551 24. Nelson, R. *et al*. Structure of the cross-β spine of amyloid-like fibrils. *Nature* **435**, 773–
552 778 (2005).
553 25. Riek, R. & Eisenberg, D. S. The activities of amyloids from a structural perspective. *Nature*
554 **539**, 227–235 (2016).
555 26. Adamcik, J. & Mezzenga, R. Amyloid Polymorphism in the Protein Folding and
556 Aggregation Energy Landscape. *Angew. Chem. Int. Ed.* **57**, 8370–8382 (2018).
557 27. Fändrich, M. *et al*. Amyloid fibril polymorphism: a challenge for molecular imaging and
558 therapy. *J. Intern. Med.* **283**, 218–237 (2018).
559 28. Qiang, W., Yau, W.-M., Lu, J.-X., Collinge, J. & Tycko, R. Structural variation in amyloid-
560 β fibrils from Alzheimer's disease clinical subtypes. *Nature* **541**, 217–221 (2017).
561 29. Liberta, F. *et al*. Cryo-EM fibril structures from systemic AA amyloidosis reveal the
562 species complementarity of pathological amyloids. *Nat. Commun.* **10**, 1–10 (2019).

30. Falcon, B. *et al*. Structures of filaments from Pick's disease reveal a novel tau protein fold. *Nature* **561**, 137–140 (2018).

31. Fändrich, M., Meinhardt, J. & Grigorieff, N. Structural polymorphism of Alzheimer Aβ and other amyloid fibrils. *Prion* **3**, 89–93 (2009).

32. Lutter, L., Serpell, C. J., Tuite, M. F. & Xue, W.-F. The molecular lifecycle of amyloid - Mechanism of assembly, mesoscopic organisation, polymorphism, suprastructures, and biological consequences. *Biochim. Biophys. Acta Proteins Proteomics* **1867**, 140257 (2019).

33. Meinhardt, J., Sachse, C., Hortschansky, P., Grigorieff, N. & Fändrich, M. Abeta(1-40) fibril polymorphism implies diverse interaction patterns in amyloid fibrils. *J. Mol. Biol.* **386**, 869–877 (2009).

34. Xue, W.-F. *et al*. Fibril Fragmentation Enhances Amyloid Cytotoxicity. *J. Biol. Chem.* **284**, 34272–34282 (2009).

35. Arosio, P., Knowles, T. P. J. & Linse, S. On the lag phase in amyloid fibril formation. *Phys. Chem. Chem. Phys.* **17**, 7606–7618 (2015).

36. Cohen, S. I. A. *et al*. Proliferation of amyloid- 42 aggregates occurs through a secondary nucleation mechanism. *Proc. Natl. Acad. Sci.* **110**, 9758–9763 (2013).

37. Jucker, M. & Walker, L. C. Self-propagation of pathogenic protein aggregates in neurodegenerative diseases. *Nature* **501**, 45–51 (2013).

38. Cohen, S. I. A. *et al*. A molecular chaperone breaks the catalytic cycle that generates toxic Aβ oligomers. *Nat. Struct. Mol. Biol.* **22**, 207–213 (2015).

39. Vidakovic, L., Singh, P. K., Hartmann, R., Nadell, C. D. & Drescher, K. Dynamic biofilm architecture confers individual and collective mechanisms of viral protection. *Nat. Microbiol.* **3**, 26 (2018).

587 40. Morris, K. L. *et al*. Exploring the sequence–structure relationship for amyloid peptides.
588 *Biochem. J*. **450**, 275–283 (2013).
589 41. Maurer-Stroh, S. *et al*. Exploring the sequence determinants of amyloid structure using
590 position-specific scoring matrices. *Nat. Methods* **7**, 237–242 (2010).
591 42. Adamcik, J., Castelletto, V., Bolisetty, S., Hamley, I. W. & Mezzenga, R. Direct
592 Observation of Time-Resolved Polymorphic States in the Self-Assembly of End-Capped
593 Heptapeptides. *Angew. Chem. Int. Ed*. **50**, 5495–5498 (2011).
594 43. Goldsbury, C., Frey, P., Olivieri, V., Aebi, U. & Müller, S. A. Multiple assembly pathways
595 underlie amyloid-beta fibril polymorphisms. *J. Mol. Biol*. **352**, 282–298 (2005).
596 44. Lara, C., Handschin, S. & Mezzenga, R. Towards lysozyme nanotube and 3D hybrid self-
597 assembly. *Nanoscale* **5**, 7197–7201 (2013).
598 45. Reynolds, N. P. *et al*. Competition between crystal and fibril formation in molecular
599 mutations of amyloidogenic peptides. *Nat. Commun*. **8**, 1338 (2017).
600 46. Noble, K. G. *et al*. Family income, parental education and brain structure in children and
601 adolescents. *Nat. Neurosci*. **18**, 773–778 (2015).
602 47. Lerch, J. P. *et al*. Studying neuroanatomy using MRI. *Nat. Neurosci*. **20**, 314–326 (2017).
603 48. Harper, J. D., Lieber, C. M. & Lansbury, P. T. Atomic force microscopic imaging of seeded
604 fibril formation and fibril branching by the Alzheimer's disease amyloid-β protein. *Chem.*
605 *Biol*. **4**, 951–959 (1997).
606 49. Dzwolak, W. Chirality and Chiroptical Properties of Amyloid Fibrils. *Chirality* **26**, 580–
607 587 (2014).
608 50. Usov, I., Adamcik, J. & Mezzenga, R. Polymorphism Complexity and Handedness
609 Inversion in Serum Albumin Amyloid Fibrils. *ACS Nano* **7**, 10465–10474 (2013).
610 51. Kundel, F. *et al*. Measurement of Tau Filament Fragmentation Provides Insights into Prion-
611 like Spreading. *ACS Chem. Neurosci*. **9**, 1276–1282 (2018).

612 52. Marchante, R. *et al*. The physical dimensions of amyloid aggregates control their infective
613 potential as prion particles. *eLife* **6**, e27109 (2017).
614 53. Takács, K., Varga, B. & Grolmusz, V. PDB_Amyloid: an extended live amyloid structure
615 list from the PDB. *FEBS Open Bio* **9**, 185–190 (2019).
616 54. Chiti, F. & Dobson, C. M. Protein Misfolding, Amyloid Formation, and Human Disease:
617 A Summary of Progress Over the Last Decade. *Annu. Rev. Biochem.* **86**, 27–68 (2017).
618 55. Hobley, L., Harkins, C., MacPhee, C. E. & Stanley-Wall, N. R. Giving structure to the
619 biofilm matrix: an overview of individual strategies and emerging common themes. *FEMS*
620 *Microbiol. Rev.* **39**, 649–669 (2015).
621 56. Wickner, R. B. *et al*. Yeast Prions Compared to Functional Prions and Amyloids. *J. Mol.*
622 *Biol.* **430**, 3707–3719 (2018).
623 57. Goedert, M., Eisenberg, D. S. & Crowther, R. A. Propagation of Tau Aggregates and
624 Neurodegeneration. *Annu. Rev. Neurosci.* **40**, 189–210 (2017).
625 58. Bousset, L. *et al*. Structural and functional characterization of two alpha-synuclein strains.
626 *Nat. Commun.* **4**, 2575 (2013).
627 59. Bateman, D. A. & Wickner, R. B. The [PSI+] Prion Exists as a Dynamic Cloud of Variants.
628 *PLOS Genet.* **9**, e1003257 (2013).
629 60. Kaufman, S. K. *et al*. Tau Prion Strains Dictate Patterns of Cell Pathology, Progression
630 Rate, and Regional Vulnerability In Vivo. *Neuron* **92**, 796–812 (2016).
631 61. Safar, J. G. *et al*. Structural Determinants of Phenotypic Diversity and Replication Rate of
632 Human Prions. *PLOS Pathog.* **11**, e1004832 (2015).
633 62. Cohen, M., Appleby, B. & Safar, J. G. Distinct prion-like strains of amyloid beta implicated
634 in phenotypic diversity of Alzheimer's disease. *Prion* **10**, 9–17 (2016).

635 63. Xue, W.-F., Homans, S. W. & Radford, S. E. Amyloid fibril length distribution quantified
636 by atomic force microscopy single-particle image analysis. *Protein Eng. Des. Sel.* **22**, 489–
637 496 (2009).
638 64. Egelman, E. H. An algorithm for straightening images of curved filamentous structures.
639 *Ultramicroscopy* **19**, 367–373 (1986).
640 65. Lutter, L., Serpell, C. J., Tuite, M. F., Serpell, L. & Xue, W.-F. Deconvolution and 3D
641 reconstruction of nano-filaments from atomic force microscopy topographs - Manuscript
642 in preparation. (2019).
643 66. Hill, S. E., Robinson, J., Matthews, G. & Muschol, M. Amyloid Protofibrils of Lysozyme
644 Nucleate and Grow Via Oligomer Fusion. *Biophys. J.* **96**, 3781–3790 (2009).

645

646

647 **Figure legends**

648

649 **Figure 1. Amyloid core models of protofilaments formed from the three Waltz peptides.**
650 Predicted models of amyloid protofilaments made from each of the 3 Waltz peptides, HYFNIF
651 (a), RVFNIM (b) and VIYKI (c). These models were generated and validated by comparing
652 simulated and experimental XRFD data as detailed in *Morris et al* [40].

653

654 **Figure 2. High resolution AFM imaging of Waltz peptide assemblies**. Fibrils generated by
655 each peptide were deposited onto freshly cleaved mica and imaged using peak force tapping
656 mode AFM. Each row shows representative image data from each assembly reaction, HYFNIF
657 (a), RVFNIM (b) and VIYKI (c). The original 6 μm by 6 μm images are shown in the left
658 column and each subsequent column shows a 2-fold increase in magnification indicated by the
659 white boxes. Different structural polymorphs are readily visible at high magnification including

different twist patterns and height profiles. The colour scale represents the height range from 0 to 12.5 nm and the scale bar represents 1 μm in all images.

Figure 3. Comparison of distinct polymorphs from straightened fibril image data. Around 90 fibrils from each data set were traced and 8 examples from each data set, HYFNIF (a), RVFNIM (b) and VIYKI (c), are displayed. The traced fibrils displayed here were straightened and cropped to 500 nm segments, and no further processing occurred. Qualitatively, each fibril can be distinguished from all of the other fibrils in each data set. Different twist patterns and average heights were readily visible. All of the fibril images analysed (around 90 fibrils for each data set) are displayed in the **Supplementary Figure SI 1**.

Figure 4. 3D models of Waltz peptide assemblies. A selection of typical reconstructed fibril 3D models is shown. Each fibril in the three data sets was reconstructed as a 3D models using information and 3D coordinates extracted directly from the AFM data. The average cross-sectional area and the helical symmetry was determined from the generation of each 3D model. Models for 8 fibrils from each assembly reaction, HYFNIF (a), RVFNIM (b) and VIYKI (c) are displayed here. The models displayed here represent the same fibrils displayed in the image data in **Figure 3**. All of the models are shown with identical scale and the colour scale represent the local radius to the screw axis for visualisation. All of the models (around 90 fibrils for each data set) are displayed in the **Supplementary Figure SI 2**.

Figure 5: Nano-morphometry on individual fibrils results in quantitative structural parameters. (a) Two example images of straightened fibrils, including a left-hand twisted fibril (left) and a right hand twisted fibril (right), are shown at the top of the figure. The corresponding height profiles across the centre line of each straightened fibril are shown below

685 them. The minimum, maximum and average heights can be determined directly from the height
686 profiles. (b) FFT of the height profiles are shown, with peaks represent the periodicity
687 describing the repeating units in the height profile. The average length covered by the repeating
688 unit, representing the periodicity of the fibrils, was extracted from this analysis. Because the
689 two example fibrils have different twist handedness, the directional periodic frequency (*dpf*)
690 was assigned as a negative value for left-hand and a positive value for right-hand twisted fibrils.
691 (c) A schematic diagram illustrating the quantitative structural parameters obtained from each
692 individual fibril. The solid black line at the bottom representing the mica surface during AFM
693 imaging. The parameters measured include the average height (h_{mean}), the minimum height
694 (h_{min}), the maximum height (h_{max}), the directional periodic frequency (*dpf*), and the cross-
695 sectional area (*csa*).
696
697 **Figure 6. Comparing the heterogeneity of the polymorphic Waltz peptide assemblies.** (a)
698 The average height of the fibrils plotted against the number of repeating units per nm, with
699 negative and positive values to distinguish handedness (directional periodic frequency, *dpf*).
700 (b) The average cross-sectional area of the fibrils plotted against the average height. The data
701 is represented as a smoothed 2D histogram and visualised as a contour map, where the
702 colouring represents the density of the data-points. The HYFNIF peptide assembly reaction
703 favours one region, whereas the RVFNIM and VIYKI data was distributed across multiple
704 regions. HYFNIF and VIYKI were also predominantly left-handed whereas the RVFNIM
705 fibrils were almost evenly split between left and right-handed. See the **Supplementary Figure**
706 **SI 4** for visualisation of the data in other pairs of structural parameters.
707
708 **Figure 7 Natural separations in the clustered data define fibril polymorph classes.** The
709 standardised Euclidean distance was measured in the 5-dimensional space between every

possible pair of fibrils in each data set and the data was separated into clusters. (a) The top row shows dendrograms in which the x-axis represents the clusters that were generated, and the y-axis is the standardised Euclidean distance between each cluster. The four data clusters with largest numbers of fibril members are indicated as circles with size corresponding to cluster size, and typical fibril structural models for each of these clusters are shown below the dendrograms. In the dendrograms, the overall distance required to cluster each entire data set reflects the overall heterogeneity of the data. (b) Scatter plot of clusters shown as spheres for directional periodic frequency vs average height where the data points are coloured dependent on the clustering at the cut-off level shown by the red line on the dendrograms above (1 standardised Euclidean distance). (c) 3D scatter plot of clusters, with directional periodic frequency vs minimum height vs maximum height with the same colouring of the clusters and projections of the various 2D plots projected onto the back walls of the plot. At this cut-off level, there were 13 clusters in the HYFNIF data set, 22 clusters in RVFNIM and 19 clusters in VIYKI with some clusters containing proportionally more of the data than others, here visualised as sphere size. Further visualisations of the hierarchical clustering analysis are shown in the **Supplementary Figure SI 5 and 6**.

729

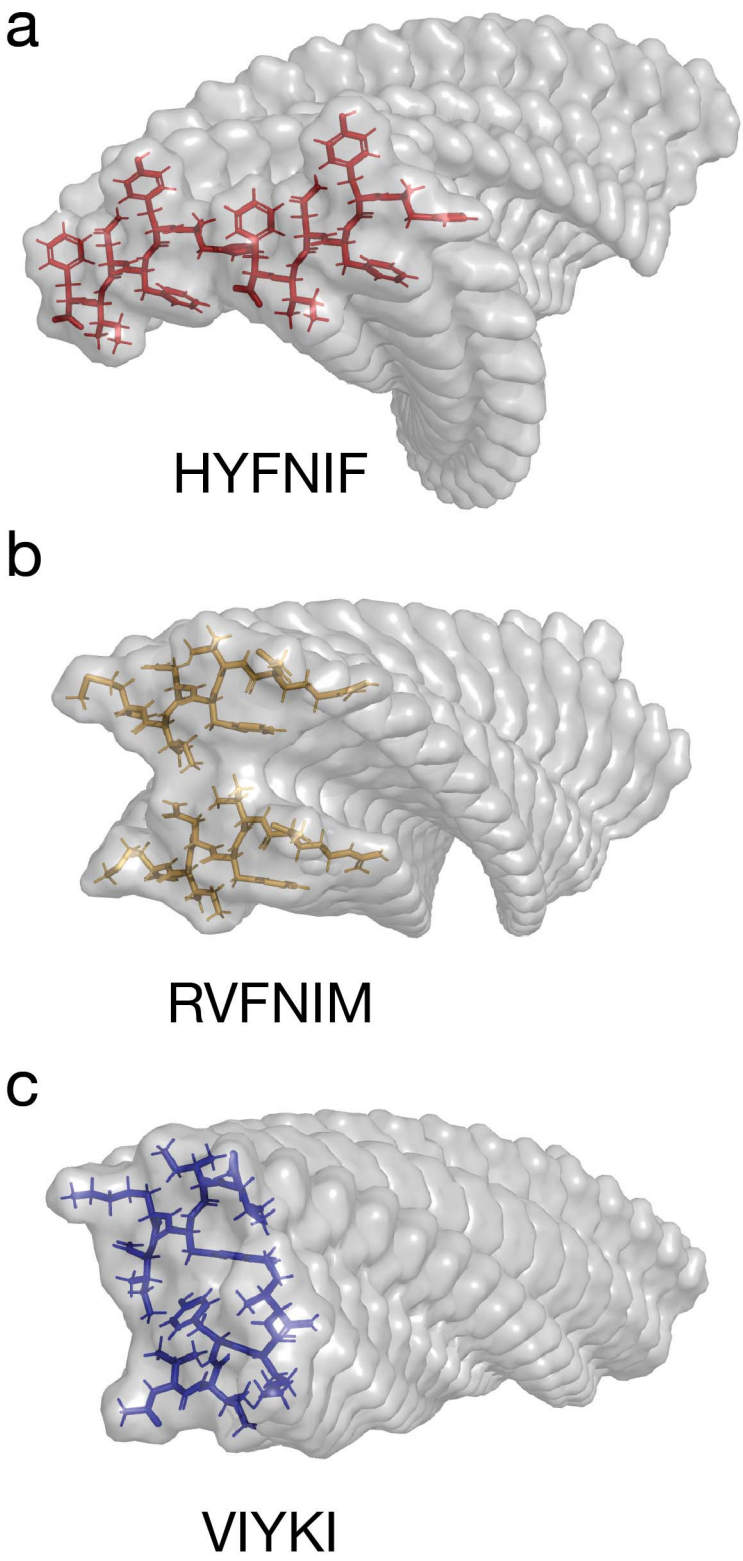

730

731 **Figure 1.**

732

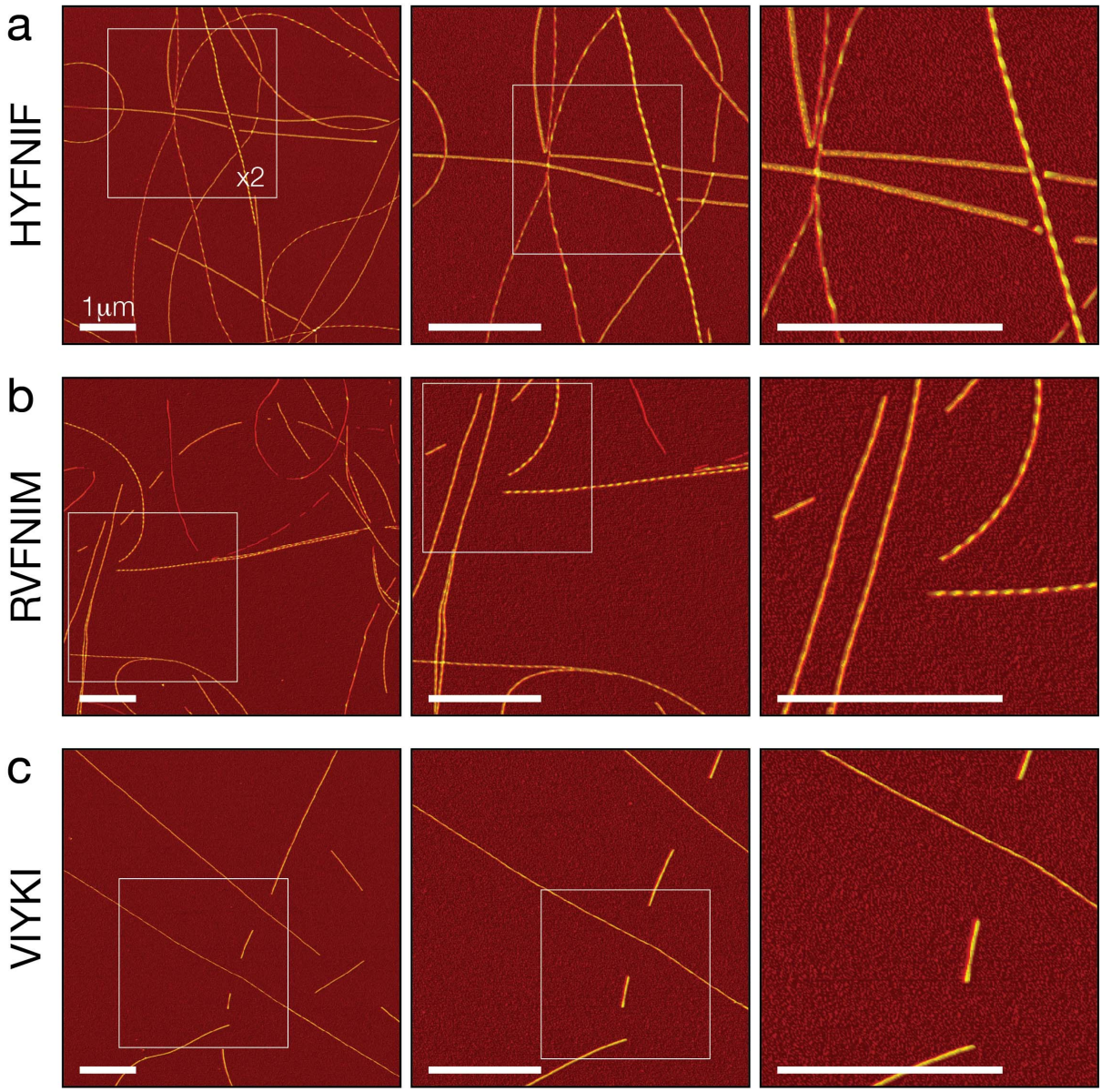

Figure 2.

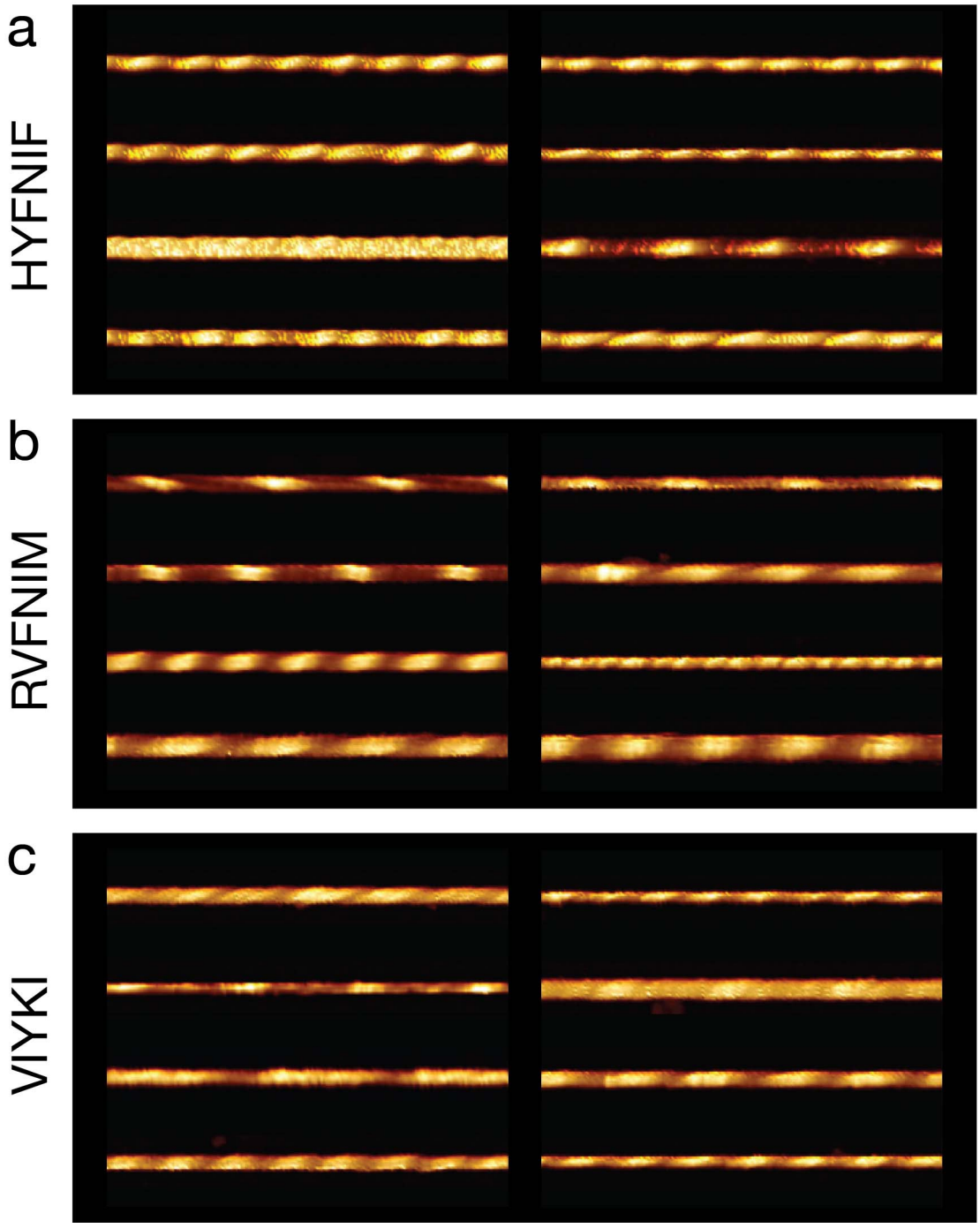

736

737 **Figure 3.**

738

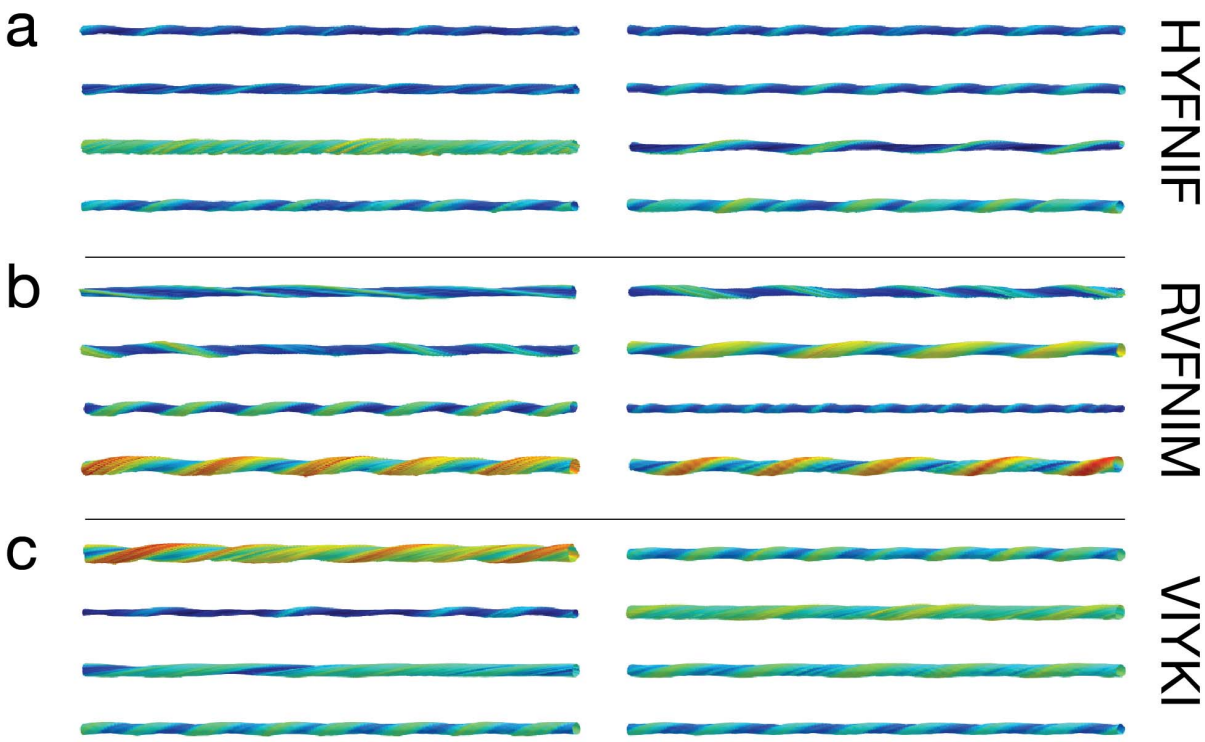

Figure 4.

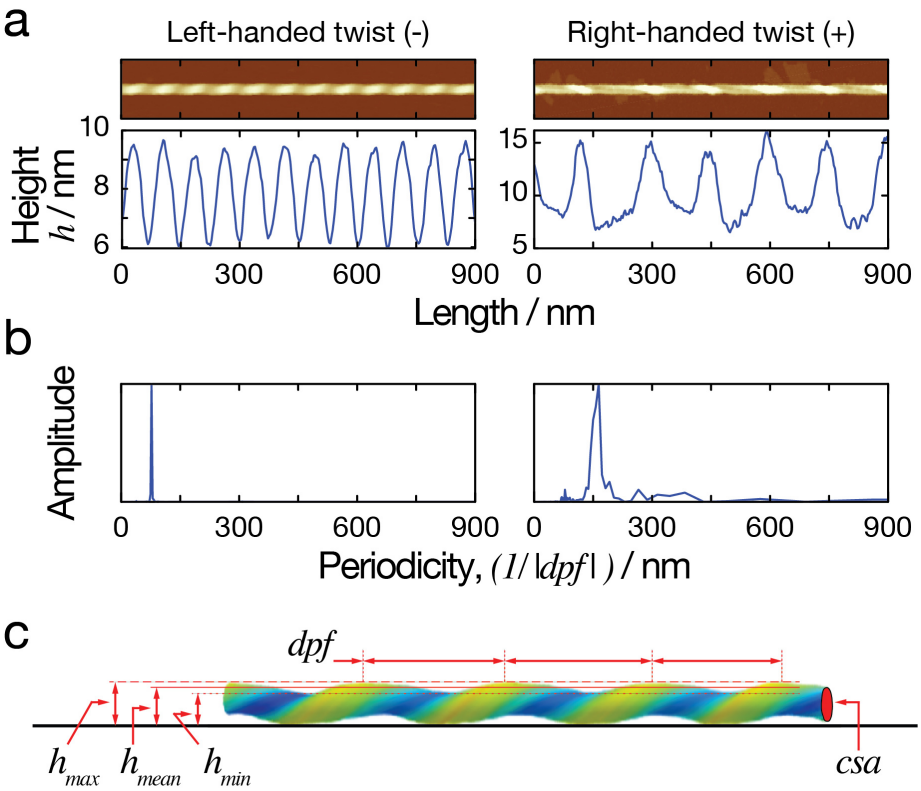

744

745 **Figure 5.**

746

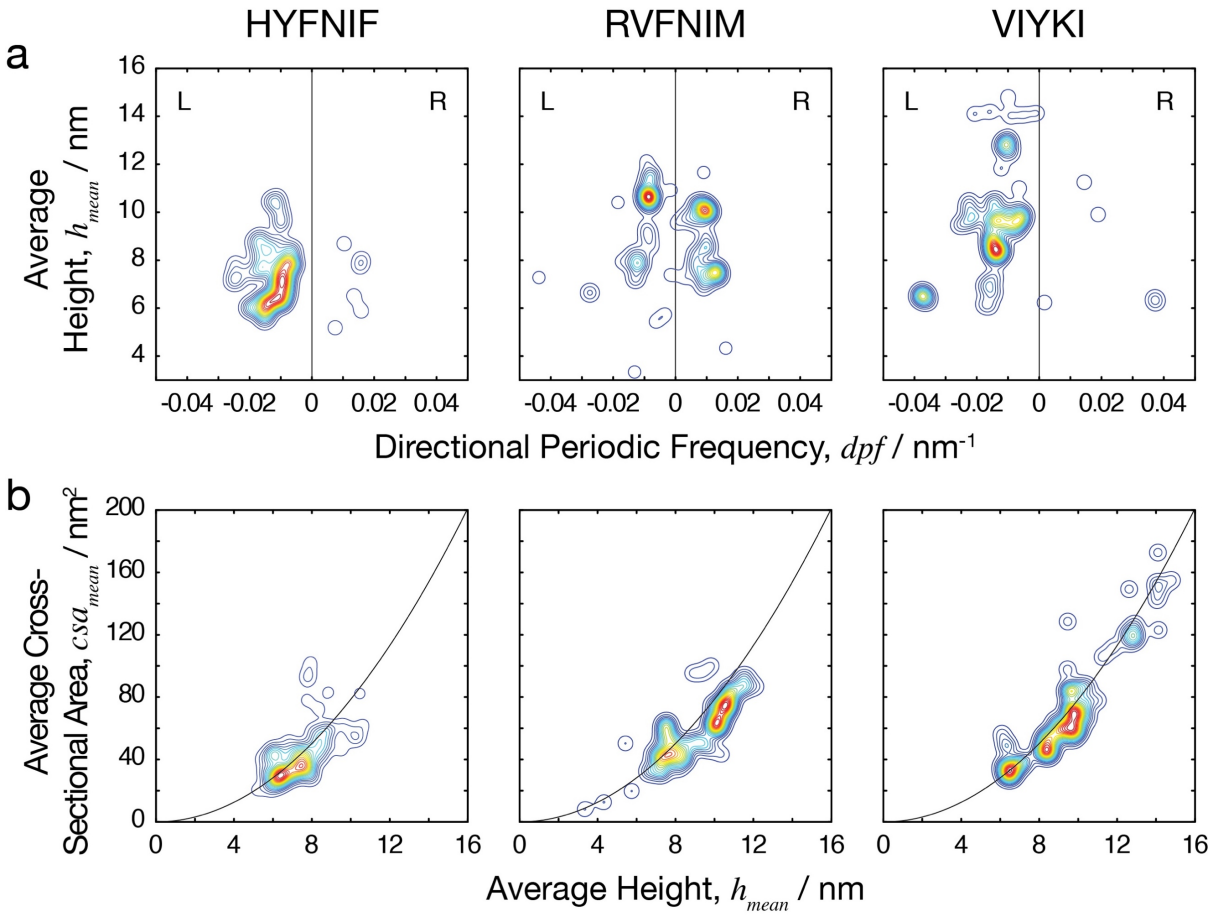

747

748 **Figure 6.**

749

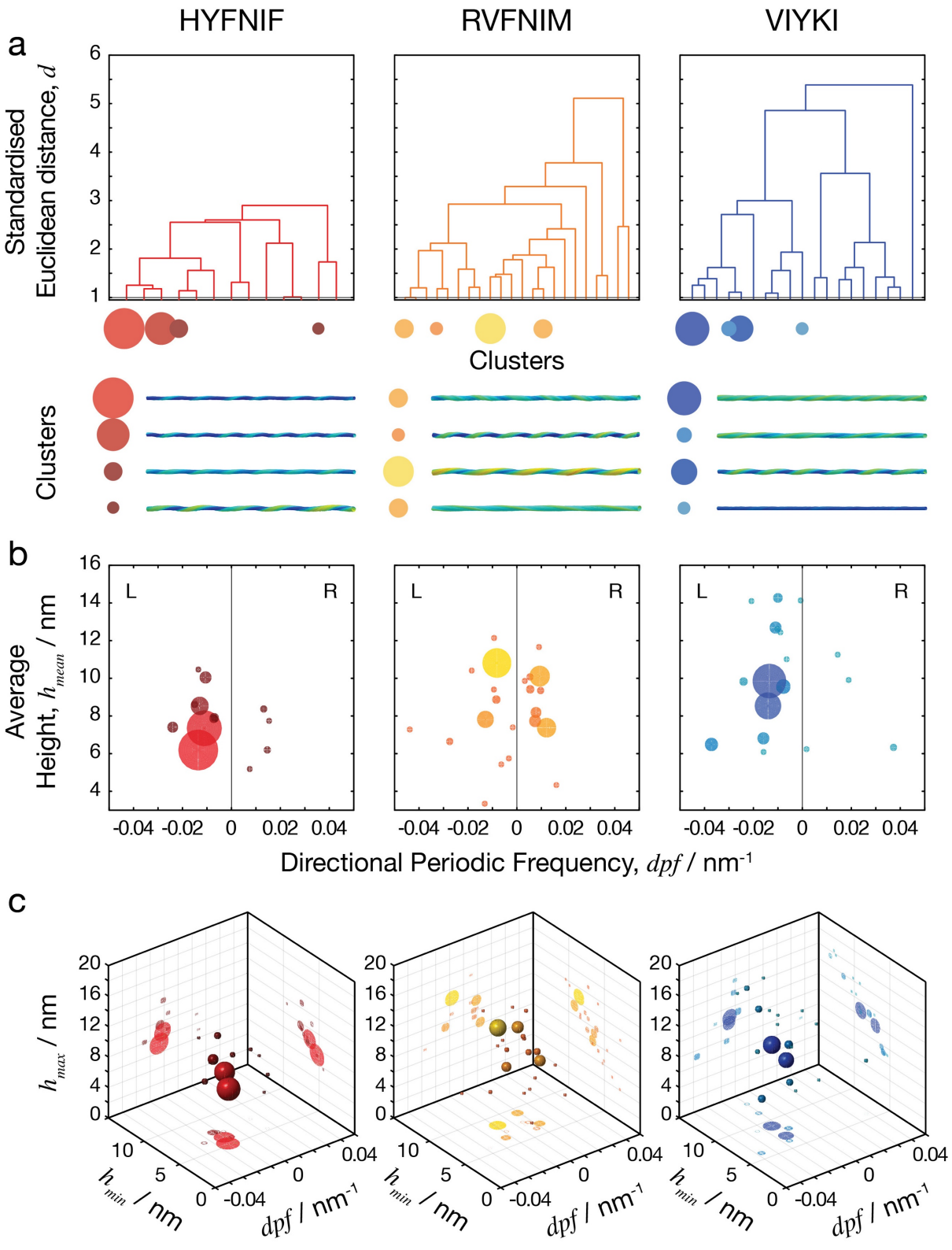

Figure 7.